USM3D Simulations for the Third Sonic Boom Workshop

Alaa Elmiligui[1], Mohagna J. Pandya[2], and Melissa B. Carter[3]
NASA Langley Research Center, Hampton VA 23681

Boris Diskin[4]
National Institute of Aerospace, Hampton, VA 23666

Sudheer N. Nayani[5]
Analytical Services & Materials, Inc., Hampton, VA 23666

The NASA USM3D flow solver was used to compute test cases for the Third AIAA Sonic Boom Prediction Workshop (SBPW3). The test cases include a nearfield biconvex shock-plume interaction wind tunnel model and the C608 Low Boom Flight Demonstrator. Numerical simulations were conducted on the mixed-element and tetrahedral grids provided by the workshop committee, as well as a family of grids generated by an in-house approach for sonic boom analyses known as BoomGrid. The nearfield pressure signatures were extracted, propagated to the ground and the perceived loudness levels on the ground were computed. The USM3D nearfield pressure signatures, corresponding ground signatures, and loudness levels on the ground are compared with that of mean values from other workshop participants. The effect of three flux-limiters on the accuracy of nearfield pressure signature prediction was investigated and results are compared with that of mean values from other workshop participants. The effect of using wall function grids in accurately predicting nearfield pressure signatures was also evaluated.

I. Nomenclature

C_p = *pressure coefficient*
$\delta P/P_\infty$ = *overpressure coefficient,* $(P - P_\infty) / P_\infty$
H/L = *distance below the model, H, normalized by model length, L*
M_∞ = *freestream Mach number*
P = *freestream pressure, psi*

---

[1] Research Engineer, Configuration Aerodynamics Branch, Mail Stop 499, AIAA Senior Member.
[2] Aerospace Engineer, Configuration Aerodynamics Branch, Mail Stop 499, AIAA Senior Member.
[3] Aerospace Engineer, Configuration Aerodynamics Branch, Mail Stop 499, AIAA Associate Fellow.
[4] Aerospace Engineer, National Institute of Aerospace, Hampton, VA, AIAA Associate Fellow.
[5] Senior Scientist, CFD Group, 107 Research Drive, AIAA Associate Fellow.

P_o / P_∞ = Engine plenum total pressure ratio to freestream static pressure
Re = *freestream unit Reynolds number, 1/in*
T_∞ = *freestream temperature, °R*
T_o = *total temperature, °R*
T_o / T_∞ = Engine plenum total temperature ratio to freestream static temperature
X = *longitudinal coordinate, m.*
y^+ = *dimensionless distance from the wall measured in terms of viscous lengths*
α = *angle of attack, deg.*
δ_1 = *height of first cell in a grid*
φ = *off-track angle, deg.*
∞ = *ambient, or freestream flow conditions*

Acronyms

AIAA = American Institute for Aeronautics and Astronautics
BC = Boundary Condition
BL = Body length
BG = Boom Grid
C608 = NASA low boom flight demonstrator
CFD = Computational Fluid Dynamics
ECS = Environment Control System
GridTool = Interactive grid/geometry setup
IGES = Initial Graphics Exchange Specification file format
HANIM = Hierarchical Adaptive Nonlinear Iteration Method
LaRC = Langley Research Center
LBPW = Low Boom Prediction Workshop
LBFD = Low boom flight demonstrator
NPR = Nozzle Pressure Ratio
PLdB = Perceived level in decibels
RANS = Reynolds-averaged Navier Stokes
RBOS = Retroreflective background oriented schlieren
SA = Spalart-Allmaras turbulence model
SBPW = Sonic Boom Prediction Workshop
STEP = Standard for the Exchange of Product Data
TetrUSS = Tetrahedral Unstructured Software System
USM3D = Unstructured tetrahedral Mesh 3D RANS solver
USM3D-ME = Mixed-element USM3D solver
VGRID = Unstructured grid generation program
WF = Wall function

Units

dB = *decibels*
ms = *milliseconds*

II. Introduction

The first Low Boom Prediction Workshop (LBPW1) was held in January 2014 in conjunction with the AIAA Science and Technology Forum and Exposition (SciTech). A summary and statistical analysis of the (LBPW1) is given in Refs. [1,2]. The workshop focused on three configurations: an axisymmetric body with a flat-top ground signature, a simple nonlifting wing body with N-wave signature, and a complex configuration with wing, tail, flow-through nacelles, and blade mount sting (LM-1021). Details of all three configurations can be found on the LBPW1 webpage [CITATION 2nd17 \l 1033]. The low boom workshop website has the listing of workshop participants and their presentations [CITATION 2nd17 \l 1033]. A follow up special session was held at AIAA AVIATION Forum 2014 where presenters and LBPW participants documented their findings [4].

In January 2017, the AIAA Applied Aerodynamics Technical Committee (APATC) conducted their second Sonic Boom Workshop (SBPW2) during the AIAA Science and Technology Forum and Exposition (SciTech 2017) to build on the success of the LBPW1. The SBPW2 was a two-day event, the first day focused on the nearfield simulation and the second day included both the nearfield simulation and the atmospheric propagation methods. The SBPW2 committee provided three required and one optional nearfield CFD test cases [5]. The test cases were an axisymmetric equivalent area body (AXIE), a JAXA wing body (JWB) [6], a NASA low boom supersonic configuration, C25D [7,8], with flow-through nacelle (C25D-F) and with propulsive engine boundary conditions (C25D-P). The surface definition of all four test cases were designed to generate, at three body lengths, similar on-track nearfield pressure signatures. A summary and statistical analysis of the SBPW2 participants' results were presented in a follow up AIAA session that was held during AIAA 2017 AVIATION Forum [9,10].

In January 2020, APATC conducted their 3rd Sonic Boom Workshop (SBPW3) during the SciTech 2020. The complexity of the SBPW3 test cases was increased to include the NASA C608 low-boom flight demonstrator (LBFD) prototype and a biconvex shock-plume interaction wind tunnel model. Details of both configurations can be found on the SBPW3 webpage [11]. The two-part workshop covered both the state-of-the-art for predicting nearfield sonic boom signatures with CFD as well as propagation of the nearfield pressures to the ground. The objectives of the workshop were to build on the success of the previous workshops; to assess the state-of-the-art computational methods as practical aerodynamics tools for predicting nearfield pressure signatures for industry relevant geometries; and to identify areas needing additional research and development. A summary and statistical analysis of the SBPW3 participants' results will be presented in four special sessions during AIAA SciTech 2021.

In the present study, the NASA Tetrahedral Unstructured Software System TetrUSS [12] with its USM3D flow solver was used to compute flowfields for the biconvex shock-plume interaction in the wind tunnel and the C608 configuration. TetrUSS has served as a reliable computational aerodynamic analysis tool for the U.S. Government and Industry for over 2 decades. The legacy Navier-Stokes flow solver within TetrUSS, USM3D, is based on fully tetrahedral cell-centered discretization. Recently, Pandya et al. [13-16], extended USM3D capability to handle mixed-element grids composed of hexahedral, prismatic, pyramidal, and tetrahedral cells, in a new version of USM3D, called mixed-element USM3D version (USM3D-ME). The extension of USM3D for multiple grid topologies has enabled its application and verification via code-to-code comparison on a wide variety of problems for which structured hexahedral grids and solutions are readily available. Using the new methodology, USM3D-ME was able to reduce time to solution up to a factor of 70 on benchmark three-dimensional

turbulent flow problems [14]. Leveraging efficient parallelization, the USM3D-ME is applied to compute solutions on grids up to 1.5 billion cells and up to 14,000 grid partitions [16]. USM3D-ME is currently being used within the NASA Commercial Supersonic Technology project, Low Boom Flight Demonstration project, and the Advanced Air Transport Technology project with the Transonic Truss-Braced Wing. The synergistic advancements to USM3D-ME have improved its accuracy and iterative and parallel efficiency providing a positive impact on the applied aerodynamicists' workflow.

The simulations for the biconvex shock-plume interaction wind tunnel model were conducted for a freestream Mach number of 1.6 and unit Reynolds number of 376,850 per inch. The nearfield pressure signatures were extracted at distances of 15 inches away from configuration and at three off-track angles, φ, of 0º, 15º, and 30º. USM3D-ME simulations for the LBFD C608 configuration were conducted for a freestream Mach number of 1.4 and unit Reynolds number of 109,776 per inch. C608 nearfield pressure signatures were extracted at three body lengths away from body, H/L=3 and at 46 off-track angles. The on-track and off-track pressure signatures were propagated to the ground and the corresponding noise levels were computed. All nearfield pressure signatures, corresponding ground signatures, loudness levels, and aerodynamic force and moment computations were uploaded to the workshop website [11].

This paper is organized as follows: (1) Description of the SBPW3 test cases; (2) Brief description of TetrUSS and USM3D-ME; (3) Description of numerical grids used in the study; (4) Presentation of the numerical results and comparison with SBPW3 participants mean results; and (5) Summary of the work and the relevant findings are presented.

III. Sonic Boom Workshop Test Cases.

The first day of SBPW3 focused on analysis of the nearfield pressure field of the biconvex and C608 configurations. The biconvex shock-plume interaction model, referred to as the biconvex model in the rest of this paper, was part of a wind tunnel test conducted at the NASA Ames Research Center (ARC) Unitary Plan Wind Tunnel (UPWT) 9- by 7-Foot Supersonic Wind Tunnel (9x7 SWT). The wind tunnel test was designed to provide a high-quality validation dataset for CFD validation. The objective of the test was to investigate the interactions between a supersonic jet plume and shock and expansion waves produced by various shock-generating surfaces. Details of the wind tunnel test can be found in Refs. [17,18]. Figure 1a shows a photograph of the model tested in the wind tunnel while Fig. 1b shows the schematic of the model used in the current numerical study. The SBPW3 technical committee provided the biconvex geometry in both IGES and STEP file format. The geometry provided is in inches. The nose is located at (x,y,z) = (0,0,0) and the model is at 3°incidence. The biconvex numerical simulations were conducted for a freestream Mach number of 1.4, unit Reynolds number of 376,850 per inch, and static temperature of 374 °R.

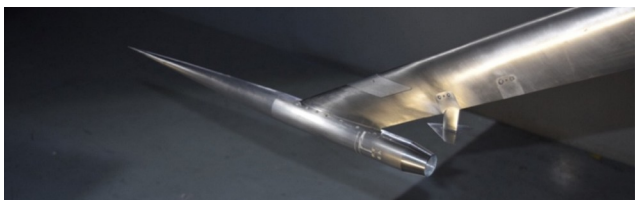

(a) Photograph of the biconvex model in NASA Ames 9x7 wind tunnel

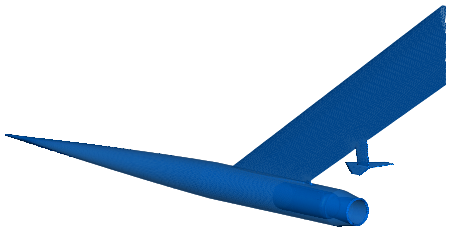

(b) Schematic of biconvex model

Figure 1 Biconvex shock plume interaction model.

The C608 LBFD configuration was the SBPW3 second test case. The C608 is an earlier version of NASA/X-59 LBFD. The C608 is more complex in terms of geometry and propulsion boundary conditions than the biconvex model. Figure 2 shows a schematic of the C608. The SBPW3 technical committee provided C608 geometry in both IGES and STEP file format. The geometry provided is in inches. The nose is located at (x,y,z) = (0,0,0). The geometry included a rotation about the nose of 2.15° to include design angle of attack. The C608 has a length of 1080 inch. The horizontal stabilator is at an incidence of +3.1° and the t-tail is at an incidence of +5.2° . The inboard flap deflection is -0.2°and aileron deflection is 0.5°.The C608 numerical simulations were conducted for a Mach number of 1.4 and at conditions corresponding to an altitude of 53,200 ft.

(a) Image of NASA/X-59 LBFD, [19] **(b) Schematic of C608 model**

Figure 2 Schematic of NASA X-59 LBFD.

IV. Computational Techniques

In this section, the details of the numerical approach and the computational grids used by USM3D-ME to compute the flowfield for the SBPW3 test cases are presented.

A. USM3D Flow Solver

The Navier-Stokes flow solver USM3D is used in the current study. USM3D was developed at the NASA Langley Research Center (LaRC). USM3D has served as a reliable computational aerodynamic analysis tool for U.S. government and Industry for over 2 decades. The preceding versions of USM3D were customized for only the tetrahedral grids. Unfortunately, the diagonal faces and skewed topology of the highly stretched tetrahedra result in a severely distorted spatial differencing stencil for computing fluxes, which may adversely affect the near-wall flow solution. Recently, USM3D has been extended to support the solutions on mixed-element grids that provide improved numerical simulation using flow-aligned anisotropic hexahedral or prismatic cells in a boundary layer and isotropic tetrahedral cells away from a boundary layer. Furthermore, additional algorithmic capabilities have been implemented that significantly improved solver robustness and time to solution. In this study, the new mixed-element USM3D code will be referred to as USM3D-ME.

A new solution methodology named Hierarchical Adaptive Nonlinear Iteration Method (HANIM) has been implemented in the USM3D-ME [15]. HANIM is a strong nonlinear solver that improves the robustness, efficiency, and automation of the RANS solutions. HANIM provides two additional hierarchies around the simple preconditioner of USM3D-ME, which is based on a linearization of a simplified discrete formulation and a point-implicit Gauss-Seidel (G-S) relaxation scheme. The HANIM hierarchies are a matrix-free linear solver for the exact linearization of the RANS equations and a nonlinear control of the solution update. The goal of these hierarchies is to enhance the iterative scheme with a mechanism for an automatic adaption of the operational pseudotime step to increase convergence rates and overcome transitional instabilities and limit cycles. The matrix-free linear solver uses the Fréchet derivatives and a Generalized Conjugate Residual method. A further enhancement to the efficiency of USM3D-ME HANIM is achieved by implementing a line-implicit preconditioner. Line-implicit iterations simultaneously update a preconditioner solution at all cells of a grid line. A line-generation algorithm suitable for general unstructured grids is developed that is solely based on local grid connectivity [16].

USM3D-ME has been parallelized for maximizing the CFD solution throughput. The parallelization is based on a Message Passing Interface (MPI) paradigm. The grid decomposition is performed internally following the current state of the art. Interpartition communication is performed judiciously and efficiently such that excellent strong scalability and weak scalability are achieved. Strong scalability is a measure of the efficiency a parallel flow solver has on a given grid when the partition size is gradually reduced, employing progressively more grid partitions. Weak scalability is a measure of how well a parallel flow solver is able to sustain its parallel efficiency when partition size is kept constant while grid size and the number of grid partitions are increased at the same rate.

Several important modifications to the discretization schemes were made to improve USM3D-ME's accuracy, efficiency, and robustness. Some of the modifications include:

- a fully-implicit formulation that is entirely based on cell-center solutions
- modification to a nodal-averaging scheme for a viable flow solver parallelization

- more consistent linearization of the target operator inside the approximate Jacobian used by the USM3D preconditioner
- an adaptive face-based catastrophic limiter
- several options for gradient limiters needed for high-speed flows
- implementation of a numerically more robust version of the negative variant of the Spalart-Allmaras turbulence model (SA-neg) that is commonly used for external aerodynamic problems
- implementation of a nonlinear quadratic constitutive relationship within the turbulent stress equations to better capture the physics of a flow problem

USM3D-ME allows for various options for computing the inviscid-flux quantities across each cell face. In the current study, the Harten, Lax, and van Leer with contact restoration scheme (HLLC) [20] was used for the inviscid flux discretization; and three types of limiters namely Barth-Jespersen, Venkat, and van Albada limiters were used to suppress numerical oscillations "wiggles" near shocks [21-23]. The effect of the limiters on nearfield pressure signature will be reported in the results section. The Spalart-Allmaras, one-equation turbulence model (SA-neg) that is commonly used for external aerodynamic problems was used to model turbulence [24-25].

B. sBOOM, Ground Propagation Code

The NASA LaRC-developed sonic-boom prediction code sBOOM was used to propagate sonic-boom signatures to the ground. sBOOM solves the augmented Burgers' equation numerically and takes into account effects such as nonlinearity, molecular relaxation, and thermoviscous absorption into the propagation process. The thickness of the shocks is predicted analytically, which avoids artificial smoothing and empirical shock thickening during loudness calculations. sBOOM can predict on-track and off-track ground signatures with or without wind effects, along with consideration for aircraft maneuvers. Further details about sBOOM and its applications can be found in Reference [26]. In this study, the Mark VII Perceived Loudness (PL) level is adopted as a measure of loudness at the ground and the LCASB loudness code is used to compute the loudness levels at the ground [27-28].

C. Computational Grids

Two sets of grids were used in this study. The first set included the tetrahedral and mixed-element grids provided by the SBPW3 committee. The SBPW3 mixed-element grids comprised of mixed tetrahedra, prisms, and pyramids while the tetrahedral grids comprised of tetrahedral cells only. SBPW3 tetrahedral and mixed-element grids were designed to have a $y^+ \leq 1$. The SBPW3 tetrahedral grids were a subdivision of the SBPW3 mixed-element grids and had the same number of nodes.

A second set of grids used in this study was the in-house set of wall-function grids for the C608 configuration. The wall-function grids were generated in order to study the effectiveness of using wall-function grids in predicting the nearfield pressure signatures. The objective was to study whether a reduction in computer time can be achieved by reducing grid resolution yet preserving accuracy in predicting nearfield pressure signatures. The next section describes the details of the biconvex and C608 grids used in the current study.

Biconvex shock plume interaction *Grids*

The SBPW3 provided a sequence of grids for both mixed-element and fully tetrahedral meshes for the biconvex model. Table 1 provides an overview of the mixed-element family of

grids, which is comprised of a sequence of three grids: coarse, medium and fine. The biconvex wind tunnel model grids are in inches, have a uniformly refined spacing in three dimensions, and are intended for $\alpha = 0°$. Table 2 provides an overview of the tetrahedra sequence of grids. The mixed-element grid size varied from a total of 3.48 million cells on the coarsest grid to 16.03 million on the finest grid level while the tetrahedral grid size varied from 4.79 million tetrahedral cells on the coarsest grid to 18.82 million on the finest grid level. USM3D-ME solutions were provided for all the grids given in Table 1. More details about the grids can be found in Refs. [11,30]. Figure 3 shows a schematic of the grid distribution for the biconvex coarse grid.

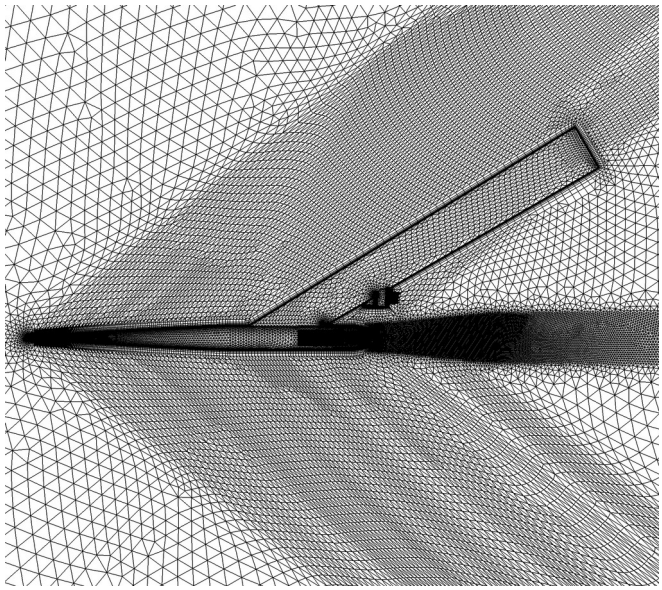

Figure 3 Schematic showing biconvex model grid distribution (coarse grid).

Table 1 SBPW3 Biconvex Family of Mixed-Element Grids.

Grid Level	Name	Scale Factor	Nodes (millions)	Cells (millions)			
				Tetrahedral	Pyramids	Prisms	Total
Bi_ME_3	Coarse	1.57	0.846	2.825	0.004	0.650	3.480
Bi_ME_2	Medium	1.28	1.576	5.985	0.006	0.993	6.985
Bi_ME_1	Fine	1.00	3.286	14.628	0.012	1.388	16.028

Table 2 SBPW3 Biconvex Family of Tetrahedral Grids.

Grid Level	Name	Scale Factor	Nodes (millions)	Tetrahedral Cells (millions)
Bi_Tet_3	Coarse	1.57	0.846	4.786
Bi_Tet_2	Medium	1.28	1.576	8.978
Bi_Tet_1	Fine	1.00	3.286	18.816

LBFD Grids

The SBPW3 provided mixed-element and fully tetrahedral sequences of grids for the C608 configuration. Table 3 provides statistics for the mixed-element family of grids while Table 4 provides statistics for the tetrahedral sequence of grids. Each family of grids is comprised of a sequence of six grids: tiny, coarse, medium, fine, extra-fine and super-fine. The C608 grids are in inches, and have a uniformly refined spacing in all three dimensions. The angle of attack of 2.15 °was designed into the geometry and the nose was set to be at (x,y,z) = (0,0,0). The mixed-element grid size varied from a total of about 30 million cells on the coarsest grid level to approximately 400 million cells on the finest grid level while the tetrahedral grid sizes varied from about 68 million tetrahedral cells on the coarsest grid to about 965 million cells on the finest grid level. USM3D solutions were provided for the first 5 grid levels of the mixed-element and tetrahedral grids. No solutions were provided for the superfine grid because the solution on the extra-fine grid was grid converged. Figure 4 shows a schematic of the C608 grid distribution. The C608 grid consisted of two parts: the inner grid, which is enclosed by the green line in Fig. 4, and the Mach aligned outer collar grid. More details about the grids can be found in Refs. [11, 31].

The wall function grids consisted of two parts: a refined inner "core grid" close to the body and a Mach-cone-aligned collar grid. The HeldenMesh software package [31] was used to generate the refined inner grid. The in-house code, Boom Grid (BG) [32], was used to generate the collar grid where cells are aligned to the freestream Mach angle.

HeldenMesh is a software system developed by the Helden Aerospace Corporation for the rapid generation of high-quality, three-dimensional, unstructured meshes about complex configurations. The software was developed to streamline the application of CFD in a demanding production environment by transforming the mesh generation process from days-per-mesh to meshes-per-day. The HeldenMesh software system consists of two primary tools: HeldenPatch and HeldenMesh. The former is the interface between the underlying computer aided design (CAD) geometry definition and the HeldenMesh grid generator. HeldenPatch includes geometry clean-up, management, and geometric transformation capabilities. An important advantage of HeldenMesh is that the software can use a GridTool restart file for mesh generation.

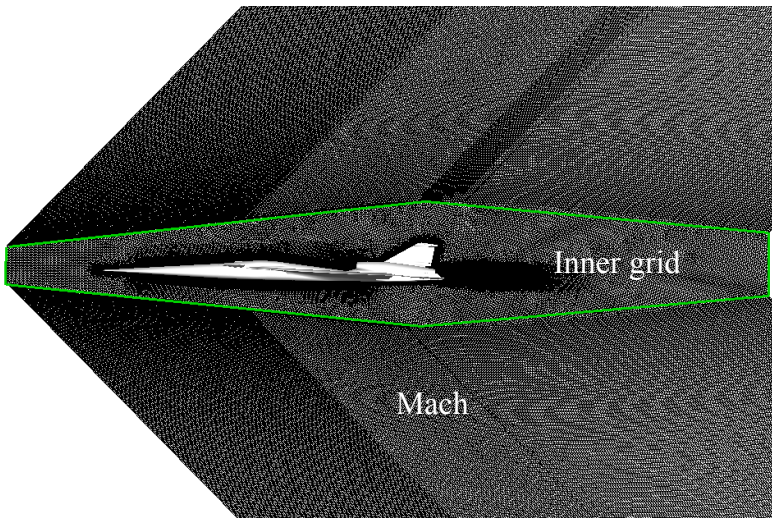

Figure 4 Schematic of the C608 SBPW3 coarse grid.

The transition between the unstructured near-body grid and the Mach-cone-aligned collar grid was made as close to the body as possible. Typically, the outer boundary is placed in such a way that there is a 0.02 × Body Length (BL) clearance between the wing tip and the outer boundary. The first cell in the collar grid was made of similar size to the adjacent core grid cell. Spacing in the radial direction increased geometrically. The collar grid geometric growth rate was scaled logarithmically similar to the boundary layer growth rate. The collar grid was swept at the freestream Mach angle with the vehicle oriented at the intended angle of attack. The collar grid extended 5000 inches from the body to allow for the extraction of signatures at 3 BL or 3240 inches, without interference from the farfield boundary reflections.

Table 5 shows statistics of the grids used in the wall-function parametric study. The wall-function grids were designed to have the first grid point off the wall located in the log-law region of the boundary layer, resulting in a grid with a much larger y^+ (an order of magnitude larger) than the SBPW3 grids. The first cell height varied from 0.0001 inches to 0.0235 inches and was the only parameter that changed. The grid sourcing was kept the same between all of the wall function grids given in Table 5.

Table 3 C608 Family of Mixed-Element Grids.

Grid Level	Name	Scale Factor	Nodes (millions)	Cell Type (millions)		
				Tetrahedral	Prisms	Total
C608_ME_6	Tiny	1.28	11.783	10.600	19.225	29.825
C608_ME_5	Coarse	1	20.701	14.682	35.347	50.028
C608_ME_4	Medium	0.8	34.879	21.267	61.008	82.274
C608_ME_3	Fine	0.64	50.215	36.568	86.084	122.651
C608_ME_2	Extra-fine	0.5	89.459	67.139	153.393	220.531
C608_ME_1	Super-fine	0.4	162.970	119.457	281.557	401.014

Table 4 C608 Sequence of Tetrahedral Grids.

Grid Level	Name	Scale Factor	Nodes (millions)	Tetrahedral Cells (millions)
C608_Tet_6	Tiny	1.28	11.783	68.487
C608_Tet_5	Coarse	1	20.701	121.015
C608_Tet_4	Medium	0.8	34.879	204.706
C608_Tet_3	Fine	0.64	50.215	295.276
C608_Tet_2	Extra-fine	0.5	89.459	527.865
C608_Tet_1	Super-fine	0.4	162.970	964.797

Table 5 C608 Details of the Grids used in Wall-Function Study.

Grid Level	First Cell Height (inch)	Nodes (millions)	Tetrahedral Cells (millions)	y^+
C608_WF_4	0.0223	33.08	197	70
C608_WF_3	0.0159	33.85	199	50
C608_WF_2	0.0069	34.90	205	25
C608_WF_1	0.0001	38.74	228	< 1

D. Boundary Conditions

The Riemann-invariant boundary condition was used along the farfield boundaries of the computational domain. The supersonic inflow boundary condition was used at the domain inflow plane and the extrapolation boundary condition was used at the downstream outflow plane of the computational domain. The no-slip viscous boundary condition was used on all solid surfaces. The symmetry boundary condition was applied at the symmetry plane of both configurations. A subsonic jet boundary condition was applied at nozzle/exhaust faces. The subsonic jet boundary condition is determined from user-prescribed values for total pressure, P_{0jet}, and total temperature, T_{0jet}. The reference quantities, the freestream conditions and the engine boundary conditions that were utilized in the numerical simulation of the biconvex and C608 are provided in and Table 7, respectively. Figure 5 shows a schematic view of the biconvex model showing the nozzle body, biconvex tail, jet boundary patch and wind tunnel probes. The jet boundary patch is colored in red in Fig. 5. Figure 6 shows the C608 power boundary conditions. The total pressure, P_{0jet}, and total temperature, T_{0jet}, values were prescribed for the engine bay ventilation face and the engine plenum face. The engine bay ventilation face is the crescent shape shown in yellow in Figure 6a while the engine plenum face is shown in red. The boundary conditions for the engine fan face and Environment Control System (ECS) were prescribed as either a constant static pressure or constant Mach number and are shown in red in Figure 6b. The effect of using the constant static pressure boundary condition versus a constant Mach number will be presented in the results section.

Table 6 Freestream and Boundary Conditions for the Biconvex model.

M_∞	1.6
α	0° (grid provided includes rotation about the nose of 3°)
T_∞	374 ° R
Re	376,850 per inch
Plenum P_o/P_∞	8.0
Plenum T_o/T_∞	1.768

Table 7 Freestream and Boundary Conditions for the C608.

M_∞	1.4
α	0° (grid provided includes rotation about the nose of 2.15°)
T_∞	389 ° R
Re	109,776 per inch
Engine fan face P/P_∞	2.8 (or alternatively M = 0.4)
Engine plenum P_o/P_∞	10.0
Engine plenum T_o/T_∞	7.0
ECS inlet face P/P_∞	1.4 (or alternatively M = 0.35)
Engine bay vent P_o/P_∞	2.4
Engine bay vent T_o/T_∞	2.0
L	1080 inches
Cruise Altitude	53,200 (ft)
Cruise Altitude	53,200 (ft)

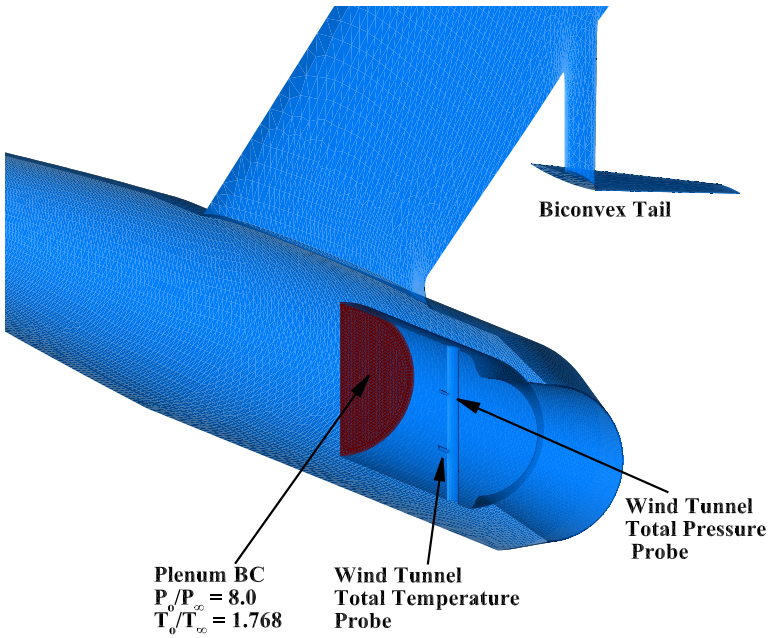

Figure 5 Schematic showing the biconvex model nozzle body, biconvex tail, jet boundary patch and wind tunnel probes.

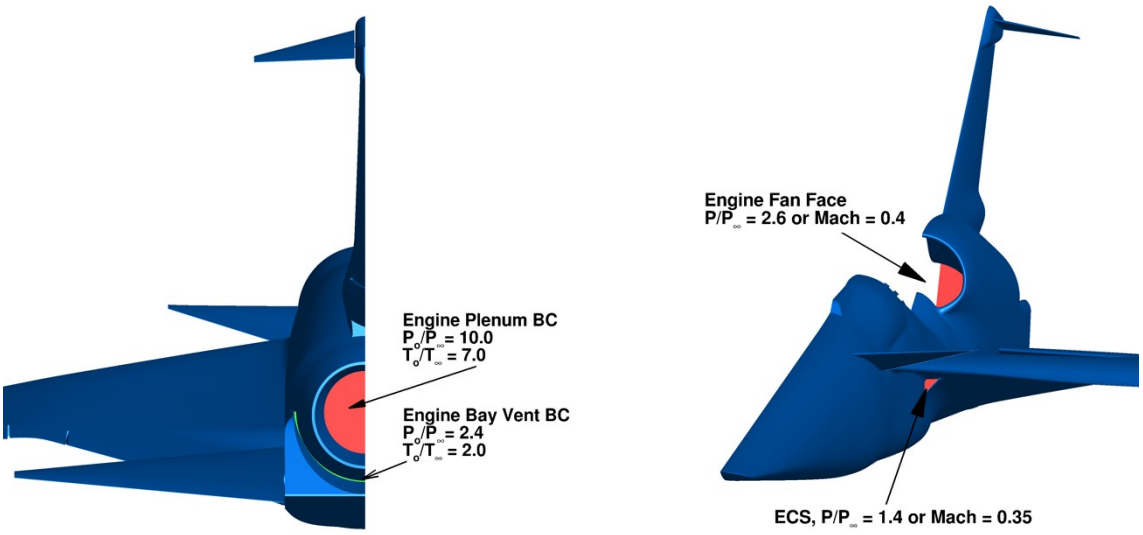

Figure 6 Schematic showing C608 power boundary conditions.

V. Results and Discussion

In this section, USM3D-ME results for the SBPW3 test cases will be presented and discussed. The biconvex simulations will be presented first followed by the C608 simulations. The nearfield pressure signatures presented in this section represent the overpressure coefficient, which is a dimensionless parameter that describes the relative pressures throughout the flowfield and is defined as $\delta P/P_\infty = (P - P_\infty) / P_\infty$. The Barth-Jespersen limiter will be the default limiter of choice unless otherwise mentioned. Effect of limiters on the nearfield pressure signature will be discussed later in this section.

The Biconvex Shock-Plume Interaction Wind Tunnel Model

The numerical simulations for the flowfield around the biconvex model were performed without tunnel walls and for a freestream Mach number of 1.6 and a unit Reynolds number equal to 376,850 per inch. The nearfield pressure signatures were extracted at distances of 15 inches away from the configuration and at three off-track angles, φ, of 0º, 15º, 30º. The simulations were performed on both the mixed-element and tetrahedral grids provided by the SBPW committee. Figure 7 shows the Bi_Tet_1 symmetry plane colored with USM3D-ME density gradient contours. The black line depicts the location of the extracted pressure signatures at 15 inches away from the model. Lines of constant density gradient extend to the far boundary. The USM3D-ME simulation was able to capture the main features of the flowfield around the biconvex model, including the nose leading shock, plume shear layer, nozzle lip shock, biconvex leading and trailing shocks as well as the refraction of the trailing biconvex shocks as it passes through the plume. Figure 8 compares the USM3D-ME results on the Bi_Tet_1 grid with the wind tunnel retroreflective background oriented schlieren (RBOS) image taken at the 9x7 SWT [17]. Figure 8 shows good agreement between the flow characteristics observed in the RBOS images and USM3D-ME density gradient contours. The grid in the wake region of the biconvex wing was coarse and hence current simulations failed to accurately capture the wake that is visible in the RBOS image.

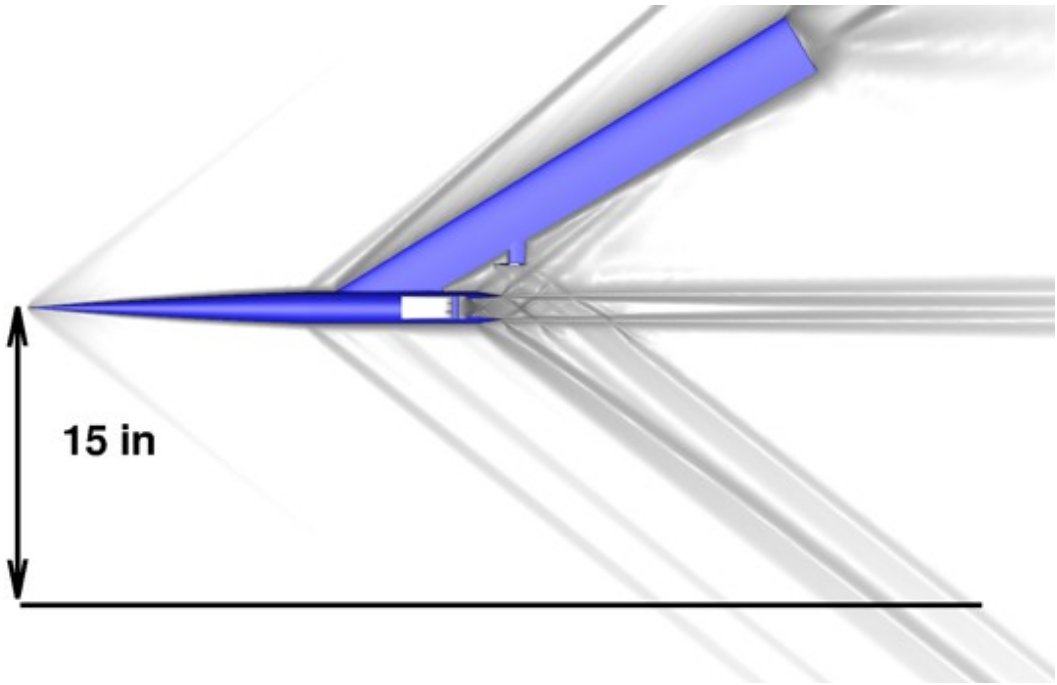

Figure 7 Symmetry plane biconvex model colored by USM3D-ME density gradient contours.
M_∞=1.6, Re = 1.6 and Re=376,850 per inch.

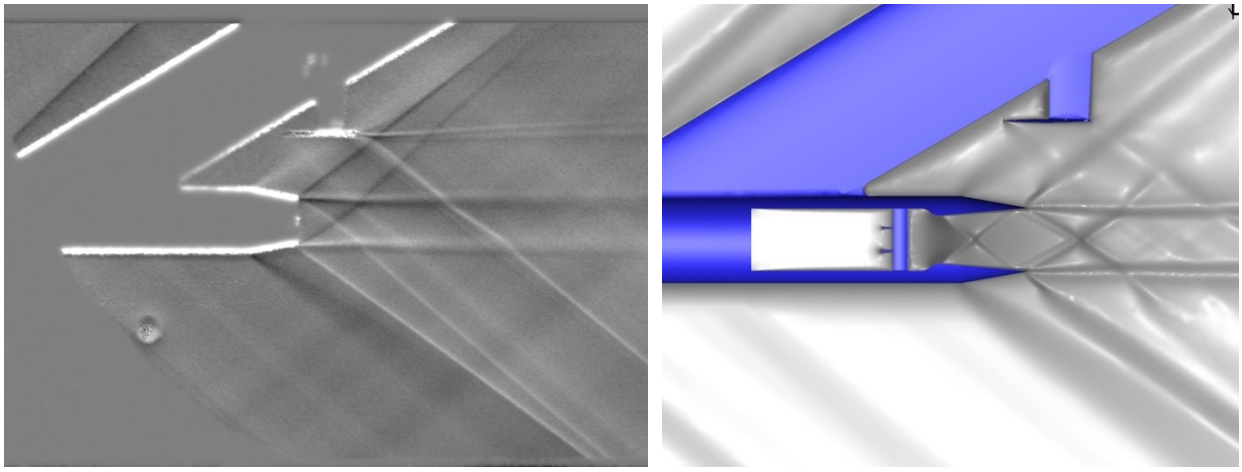

(a) RBOS *dY* image, *NPR* = 8, Ref. [17]

(b) USM3D-ME density gradient contours

Figure 8 Comparison of RBOS and USM3D-ME density gradient for the biconvex model.

Figure 9 shows a comparison of USM3D-ME on-track overpressure signatures for each of the grids given in Table 2. Figure 9 visually shows that the predicted overpressure signatures are grid converged. Figure 10 shows USM3D-ME off-track nearfield pressure signatures on the Bi_Tet_1 grid. The off-track signatures are in agreement on the front part of the body where the flow is compressive and in the axial direction. The blade perturbs the axial flow pattern and

results in a slight shift in the off-track pressure signatures. The biconvex leading and trailing shocks slightly shift the off-track signatures from the on-track signature at and just downstream of the lip-shock as shown in Fig. 10. Figure 11 shows a comparison of the USM3D-ME on-track overpressure signatures on the SBPW3 medium grid level of the mixed-element and tetrahedral grids. As expected, the USM3D-ME signatures on both grids are overlaying because simulations converged to machine zero and both types of grids have the same node distribution. Figure 12 shows the comparison of USM3D-ME and workshop mean nearfield pressure signatures. The USM3D-ME results are in excellent agreement with workshop mean nearfield pressure signatures. In the present study, the effect of three limiters on the nearfield overpressure signatures were investigated. Figure 13 shows the effect of Barth-Jespersen, Venkat and van Albada limiters on the nearfield overpressure signatures predicted by USM3D-ME. The nearfield overpressure signature predicted by the three limiters are in good agreement in the front part of the signature and predictions slightly differ in the aft part of the signature. The largest difference can be seen at and just downstream of the lip-shock, X ~ 42.4 in, and downstream of the trailing-edge shock, X ~ 46.2 in. Figure 13 depicts that the Venkat limiter overpredicted the pressure rise of the nozzle lip shock and that the Barth-Jespersen limiter is more in agreement with the SBPW3 mean nearfield pressure signatures.

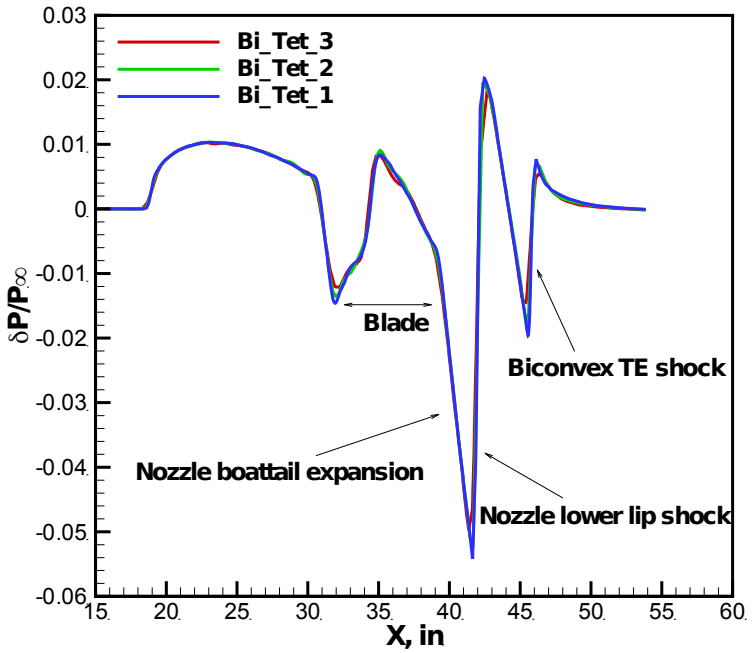

Figure 9 USM3D-ME nearfield overpressure signatures on the SBPW3 tetrahedral grids at M_∞=1.6, α=0.0°, and Re=376,850 per inch.

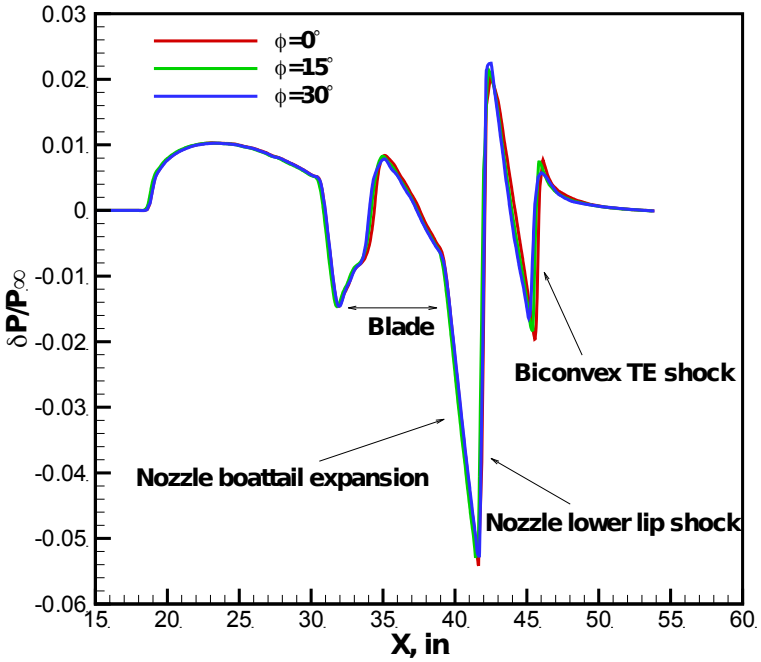

Figure 10 **USM3D-ME nearfield overpressure off-track signatures on the SBPW3 tetrahedral Bi_Tet_1 grid at M_∞=1.6, α=0.0º, and Re=376,850 per inch.**

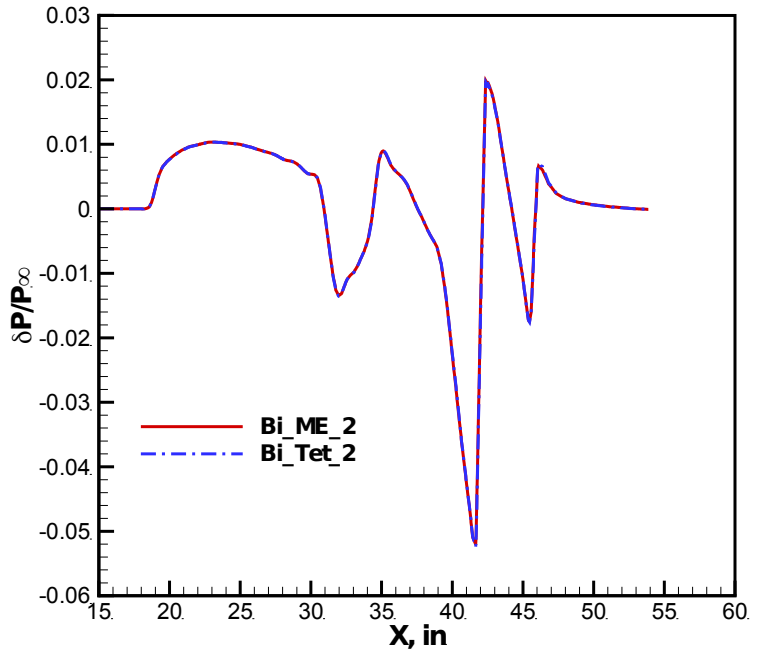

Figure 11 USM3D-ME nearfield overpressure signatures on the SBPW3 mixed-element and tetrahedral grids at M_∞=1.6, α=0.0º, and Re=376,850 per inch.

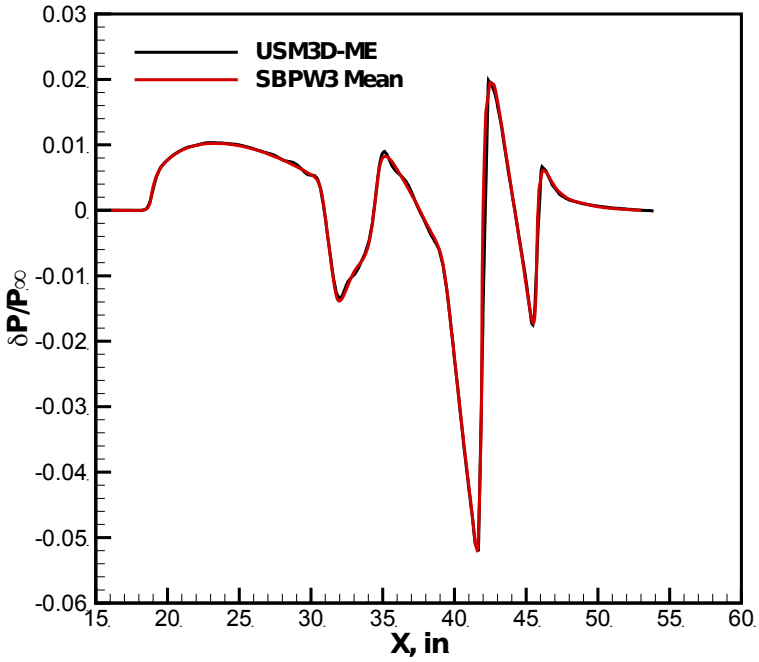

Figure 12 Comparison of USM3D-ME nearfield pressure signatures with the SBPW3 participants' mean nearfield pressure signatures at M_∞=1.6, α=0.0°, and Re=376,850 per inch.

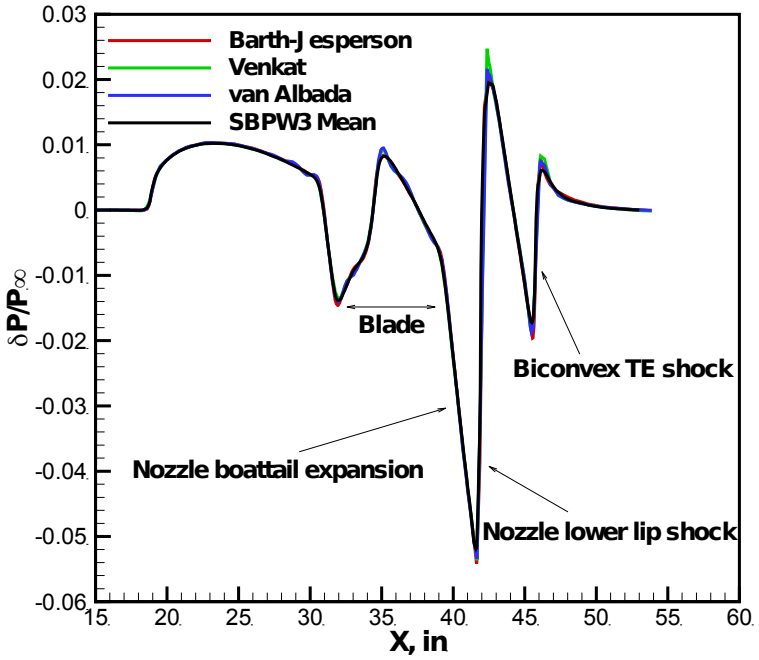

Figure 13 Effect of limiters on the nearfield overpressure signatures predicted by USM3D-ME at M_∞=1.6, α=0.0°, and Re=376,850 per inch.

C608 Low Boom Flight Demonstrator

The C608 LBFD is an early version of the NASA X-59 Low Boom Flight Demonstrator [19]. The C608 configuration is more complex in terms of geometry and propulsion boundary conditions than the biconvex configuration. It is also more representative of vehicles with lower ground loudness. A schematic of the C608 was given in Figure 2. USM3D-ME C608 simulations were conducted at M_∞ = 1.4, α = 0.0° and *Re* = 109,776 per inch. The nearfield overpressure signatures were extracted and propagated to the ground with the atmospheric propagation code, sBOOM. The USM3D nearfield pressure signatures, corresponding sBOOM ground signatures, and loudness levels on the ground are compared with mean values from other workshop participants.

The grids provided by the SBPW3 committee included a rotation of 2.15°, about the nose, to include the C608 design angle of attack. USM3D-ME C608 simulations were performed on both the SBPW3 mixed-element and purely tetrahedral grids. The simulations were conducted on the five coarsest grid levels. There was no need to run on the extra-fine grid level as the solution was fully grid converged by the fifth grid level, C608_ME_2 & C608_Tet_2. USM3D simulations where also conducted on a series of in-house wall function grids in order to evaluate the effectiveness of using wall function grids in capturing nearfield overpressure signatures. Details of the wall function grids was given in Table 5. The legacy USM3D code was used in the wall function grid study.

Figure 14 shows a USM3D-ME surface pressure distribution for the C608 configuration. Figure 15 shows a close-up view of the Environment Control System (ECS). The shock emanating from the ECS vent wraps around the lower surface of the wing as shown by the red colored band in Fig. 15. Figure 16 shows contours of nearfield overpressure signatures at three body lengths away from the C608. The black lines depict the location of the extracted pressure signatures at 3 body lengths away from the C608. The SBPW3 committee requested to extract off-track signatures every 2°in the azimuthal direction, i.e., total of forty-six off-track angles.

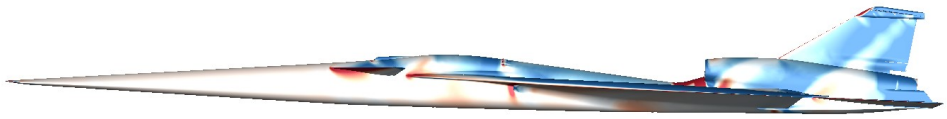

(a) Side view

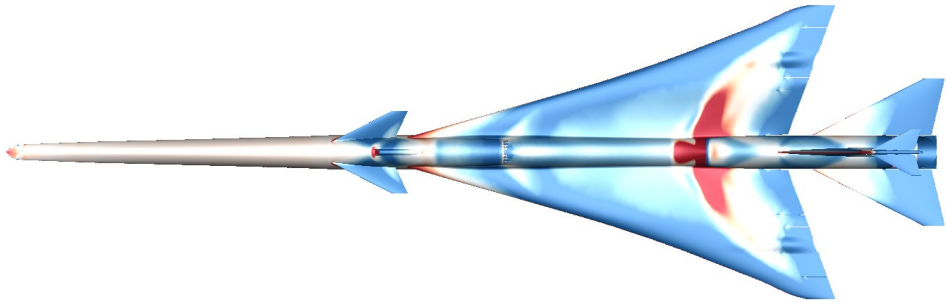

(b) Upper surface.

Figure 14 **USM3D-ME surface pressure coefficient for the C608 at M_∞=1.4, α = 0.0°, and *Re=109,776 per inch.***

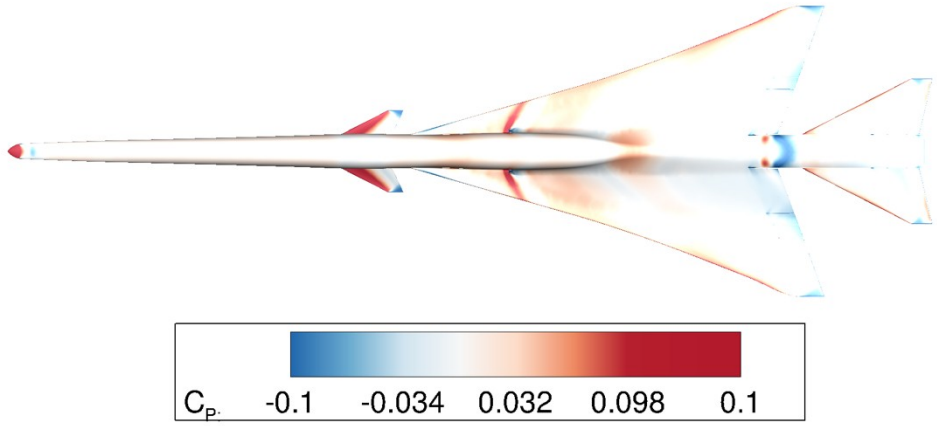

(a) Lower Surface

Figure 15 USM3D-ME surface pressure coefficient showing shock in front of ECS at M_∞*=1.4,* α *= 0.0°,* and *Re=109,776 per inch.*

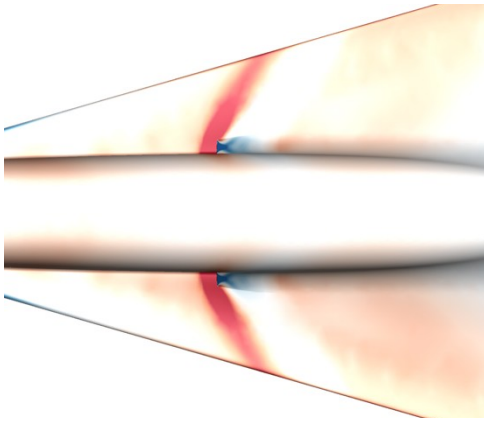

Figure 15 Continued (blow up of the ECS).

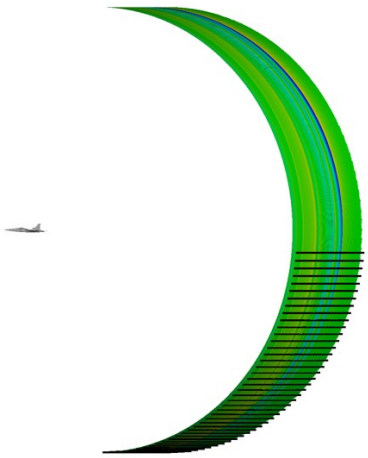

Figure 16 USM3D-ME computed overpressure contours at three body lengths away from the C608 at ***M_∞=1.4, α = 0.0°,*** **and** ***Re=109,776 per inch***

Figure 17a shows a comparison of USM3D-ME on-track overpressure signatures on each of the SBPW3 mixed-element grids. Figure 17a shows that the predicted overpressure signatures are grid converged. The simulations on all grid levels, with the exception of the coarsest grid level "C608_ME_1" that was not included here, captured consistently all flow features and shock locations. The nearfield pressure signatures were extracted at H/L =3 and were all propagated to the ground using sBOOM. Figure 17b shows the nearfield overpressure signatures on the ground and the corresponding PLdB noted in the legend. Figure 17b depicts that the C608 on-track ground signatures are grid converged. The difference in the PLdB levels between on-track ground signatures shown in Figure 17b is less than 0.2 dB. Figure 17c shows the predicted carpets of PLdB. If we eliminate the results from the coarsest grid level, we find that the difference in the PLdB levels between ground signatures shown in Figure 17c is less than 1 dB. Figure 17c illustrates that the solutions are grid converged and the difference in PLdB on the two finest grid levels is less than 0.2 dB. All predicted nearfield overpressure, ground signatures and corresponding PLdB levels were uploaded to the SBPW3 website [11].

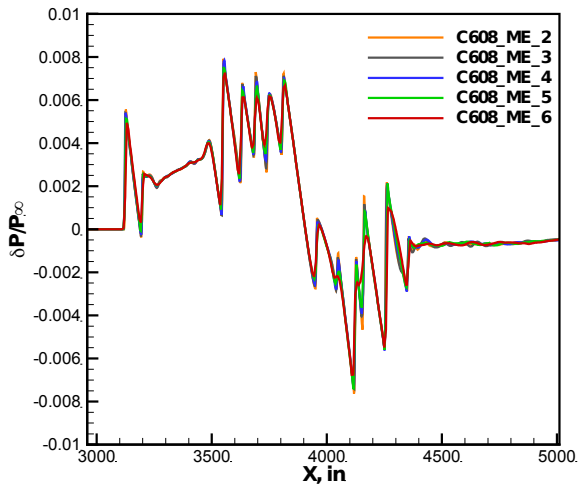

(a) Nearfield overpressures extracted at H/L = 3

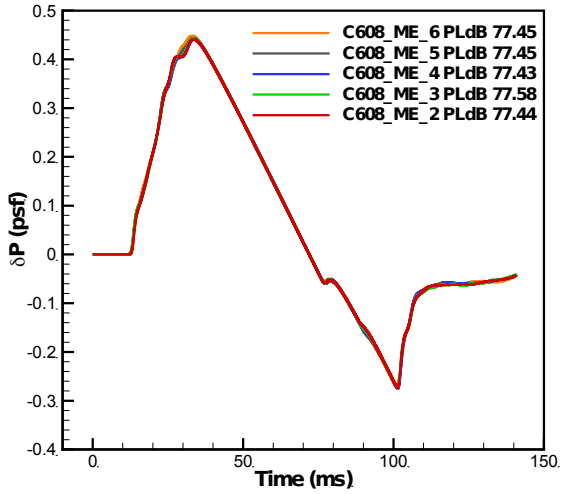

(b) Ground signatures

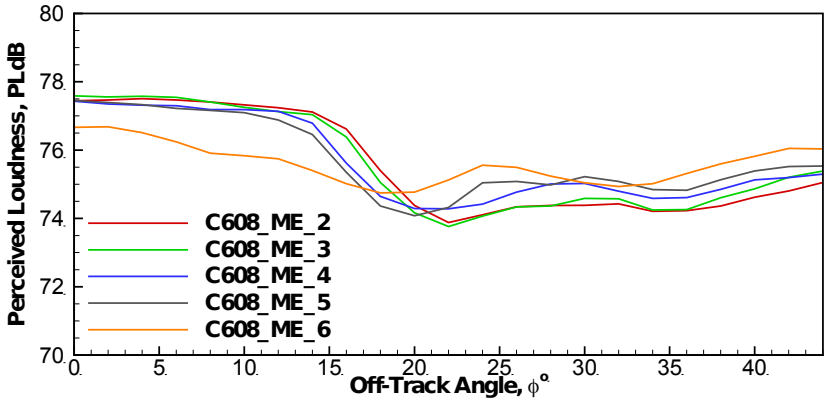

(c) Carpet of perceived loudness level

Figure 17 USM3D-ME simulations for the C608 configuration on the SBPW3 mixed-element grids at M_∞=1.4, α = 0.0°, and *Re=109,776 per inch.*

Figure 18a shows comparisons of the USM3D-ME on-track nearfield overpressure signatures as predicted on the fine grid level of the mixed-element grid (C608_ME_3), the all tetrahedral grid (C608_TE_3), and the SBPW3 participants' mean. As expected, the USM3D-ME nearfield overpressure signatures, red and blue lines in Fig 18a, are identical because USM3D-ME simulations are converged to machine zero and both types of grids have the same node distribution. Figure 18a depicts that there is good agreement in capturing the shock locations between USM3D-ME on-track nearfield overpressure signatures and SBPW3 participants' mean, however, USM3D-ME yielded slightly stronger and sharper shocks. Figure 18b shows predicted PLdB levels on the ground. The front and aft part of the carpet shows good agreement between USM3D-ME predictions and the SBPW3 mean. The agreement deteriorates between off-track angles $12° < \varphi < 24°$. The carpet of predicted PLdB levels fell within one standard deviation band of the ensemble data. The bars shown in Fig. 18b are the standard deviation of the SBPW3 ensemble data and they extend one standard deviation vertically from the mean.

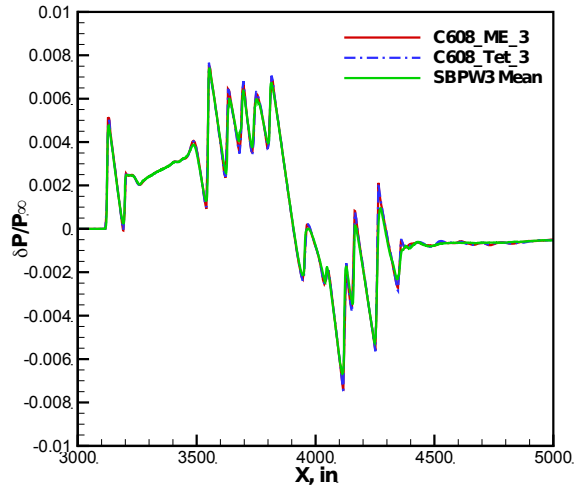

(a) Predicted nearfield overpressure signatures

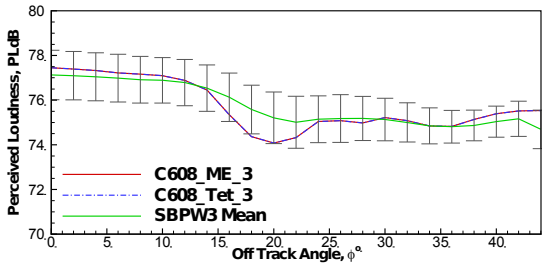

(b) Carpet of predicted PLdB levels

Figure 18 **Comparison between USM3D-ME predictions and SBPW3 mean at** M_∞***=1.4, α = 0.0°, H/L=3,* and *Re=109,776 per inch.***

The effect of limiters on the prediction of nearfield overpressure signature was examined. The Barth-Jespersen, Venkat and van Albada limiters were used to predict C608 nearfield overpressure signatures. Figure 19 shows that the on-track nearfield overpressure signature predicted by the three limiters. The signatures are in good agreement in terms of capturing the shock location, however, each limiter yielded different shock peaks. The Venkat limiter has the least amount of dissipation and hence yielded the highest shock peaks as compared to the van Albada and Barth-Jespersen limiters. Figure 19b shows carpets of the PLdB levels as predicted by the three limiters. The spread in PLdB levels due to the use of different limiters is less than 0.2 dB.

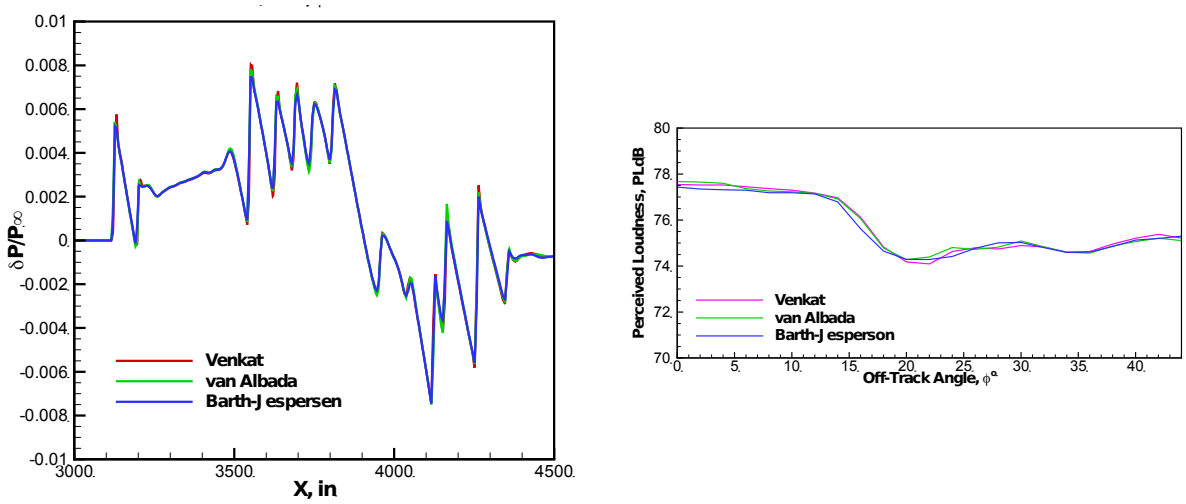

(a) Predicted on-track nearfield overpressure signatures

(b) Carpet of predicted PLdB levels

Figure 19 **Effect of limiters on USM3D-ME predictions at** M_∞***=1.4,*** α ***= 0.0°, H/L=3,* and *Re=109,776 per inch.***

The SBPW3 committee offered workshop participants two types of BCs for the ECS inlet face and the engine fan face. Figure 20 shows the effect of specifying a prescribed Mach number at both faces, versus using a prescribed static pressure. The black line in Figure 20a depicts a signature with constant Mach number while the red line is a signature with a prescribed static pressure at the boundary face. The signatures are in good agreement with some discrepancy at around X ~ 3700 inch, which correlates with the ECS shock location. Figure 20a illustrates that the fan face BC type had no effect on the prediction of the on-track overpressure signature. This is probably due to the fact that any discrepancy in the flowfield due to the engine fan face BC was shielded by the C608 wing. Figure 20b shows the effect of both types of BCs on the predictions of PLdB levels on the ground. The PLdB levels are in good agreement up to an off-track angle of ~ 22°. The spread in PLdB levels due to the use of different BCs is less than 0.5 dB.

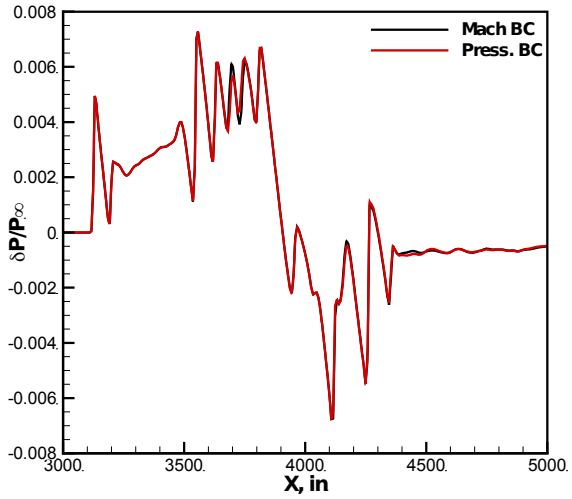

(a) Predicted on-track nearfield overpressure signatures

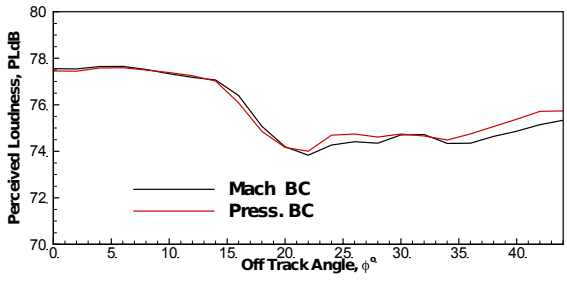

(b) Carpet of predicted PLdB levels

Figure 20 Effect of the type of BC on USM3D-ME predictions at M_∞=1.4, α = 0.0°, H/L=3, and Re=109,776 per inch.

The authors conducted a study to examine the effectiveness of using wall function (WF) grids in predicting nearfield overpressure signatures. The objective of the study was to conduct a preliminary investigation to determine whether a reduction in computing requirements can be achieved by using WF grids while preserving the integrity of the signatures. A family of in-house grids were generated where y^+ varied from 0.1 to 70. Details of the grids were provided in Table 4. The grid sourcing was the same on all four grids used in the WF study. The only difference between WF grids was in the first cell height. The legacy USM3D production code was used in the WF study. The nearfield overpressure signatures where extracted from the USM3D simulations, and the corresponding ground signatures and the PLdB levels on the ground were computed and compared to the mean from the SBPW3 ensemble of data. Figure 21a shows the USM3D on-track nearfield overpressure signatures, extracted from three body-lengths away from C608 on the WF grids. Figure 21a illustrates that the front portion of the signatures are in good agreement with signatures overlaying on each other, however, discrepancies can be viewed at the aft part of the signature, plume region, at an X location ≥ 4300 inches. Figure 21b shows the on-track 608 ground signatures propagated from the USM3D simulations on the WF grids. The comparison shows qualitatively good agreement with slight discrepancies from predictions on the C608_WF_4 grid**.** The difference in perceived loudness level between on-track signatures is less than 0.5 dB. Figure 20c shows comparisons between carpets of the PLdB levels as predicted by USM3D on the WF grids and the SBPW3 participants' mean. The spread in PLdB levels due to the use of WF grids is less than 1 dB and is within one standard deviation band of SBPW3 ensemble of data. WF grids provide a viable option to compute nearfield pressure signatures. However, if interest is to compute the forces and moments as well as nearfield pressure signatures, the authors recommend the use of grids with $y^+ < 1$.

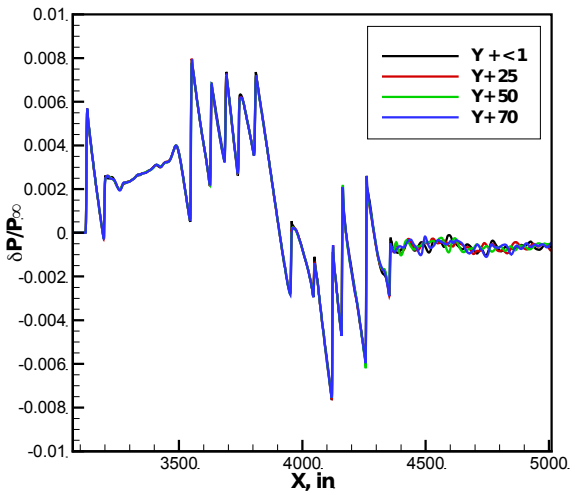

(a) Nearfield on-track overpressure signatures

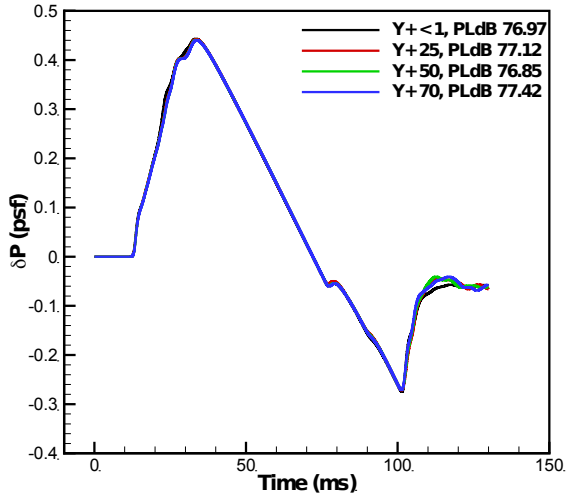

(b) On-track ground signatures

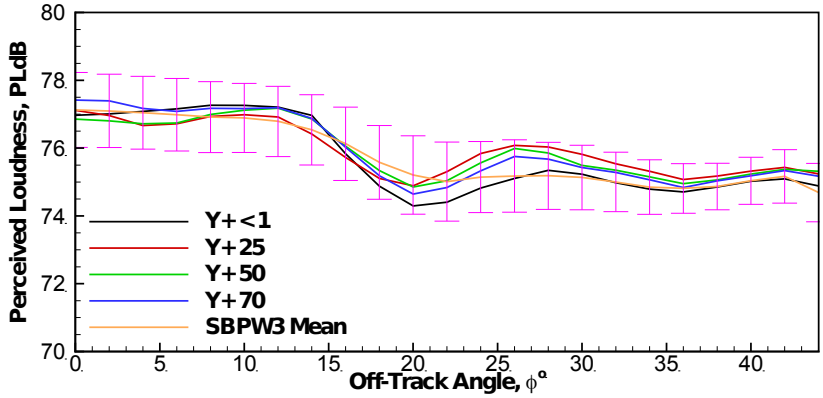

(c) Carpet of perceived loudness level

Figure 21 USM3D-ME C608 simulations on the wall function grids at M_∞=1.4, α = 0.0°, H/L=3, and ***Re=109,776 per inch.***

VI. Summary

This paper presented the USM3D results for the Third AIAA Sonic Boom Prediction workshop. The SBPW3 included a nearfield biconvex shock-plume interaction wind tunnel model and the NASA C608 low-boom aircraft. The USM3D-ME Navier–Stokes solver was used to compute the fully turbulent flow around both configurations using the HLLC approximate Riemann solver for inviscid flux discretization and the negative variant of the Spalart-Allmaras turbulence model (SA-neg) to model turbulence.

USM3D-ME simulations for the biconvex model were conducted for a freestream Mach number of 1.6, and unit Reynolds number equal to 376,850 per inch. The nearfield pressure signatures were extracted at distances of 15 inches away from the configuration and at three off-track angles, φ, of 0º, 15º, and 30º. The simulations were performed on both the mixed-element and tetrahedral grids provided by the SBPW3 committee. USM3D-ME biconvex results showed that the predictions were grid converged. The predicted nearfield pressure signatures were extracted and compared with the mean from SBPW3 participants ensemble of data. The

comparison showed excellent agreement between USM3D-ME predictions and the mean from the SBPW3 ensemble of data.

USM3D-ME simulations for C608 were conducted for a freestream Mach number of 1.4, α of 2.15º and unit Reynolds number equal to 109,776 per inch. The nearfield pressure signatures were extracted at three body lengths away from the C608 configuration. The off-track signatures were extracted every 2º in the azimuthal direction, up to φ=90º. The simulations were performed on both the mixed-element and tetrahedral grids provided by the SBPW committee as well as on a family of in-house BG grids. USM3D-ME results for the C608 configuration showed that the predictions were grid converged. The predicted nearfield pressure signatures were propagated to the ground using the NASA propagation code sBOOM. The loudness levels at the ground were computed by the LCASB loudness code. The comparison showed good agreement between the USM3D-ME predictions and the mean from the SBPW3 ensemble of data.

The Barth-Jesperson, Venkat and van Albada limiters were used in the current study to evaluate their effectiveness in predicting the turbulent flowfield for both the biconvex and C608 configurations. Predictions from all three limiters were in good agreement with the SBPW3 mean. The Venkat limiter had the least amount of numerical dissipation and resulted in the strongest shocks. The Barth-Jesperson limiter was more in agreement with the SBPW3 mean. All three limiters were within one standard deviation band of the SBPW3 ensemble of data.

The authors conducted a study to examine the effectiveness of using WF grids for sonic boom computations. A family of in-house grids were generated for this purpose, where y^+ varied from 0.1 to 70. The legacy USM3D production code was used in the WF study. The nearfield pressure signatures were extracted from the USM3D simulations and the ground signature and the corresponding PLdB levels on the ground were computed. The PLdB levels predicted from the WF grids were within one standard deviation band of the SBPW3 ensemble of data. WF grids provide a viable option to compute nearfield pressure signatures. However, if interest is to compute forces and moments as well as nearfield pressure signatures, authors recommend the use of grids with $y^+ < 1$.

Acknowledgments

The research reported in this paper was sponsored by the NASA Commercial Supersonic Technology Project.

References

[1] Park, M. A. and Morgenstern, J. M., "Summary and Statistical Analysis of the First AIAA Sonic Boom Prediction Workshop", 32nd AIAA Applied Aerodynamics Conference, AIAA AVIATION Forum, (AIAA 2014-2006).

[2] Morgenstern, J. M., "Measurements Supporting 1st Sonic Boom Prediction Workshop Cases", 32nd AIAA Applied Aerodynamics Conference, AIAA AVIATION Forum, (AIAA 2014-2007).

[3] AIAA Low Boom Prediction Workshop, Available: https://lbpw-ftp.larc.nasa.gov/lbpw1 [Accessed March 2020].

[4] AIAA Aviation 2014 Low Boom Special Session, Available: https://lbpw-ftp.larc.nasa.gov/aviation-2014 Accessed March 2020].

[5] AIAA Second Sonic Boom Workshop, Available : https://lbpw-ftp.larc.nasa.gov/sbpw2.

[6] Ueno, A., Kanamori, M., and Makino, Y., “Multi-fidelity Low-boom Design Based on Near-field Pressure Signature,” AIAA Paper 2016–2033, 2016.
[7] Wintzer, M., Ordaz, I., and Fenbert, J. W., "Under-Track CFD-Based Shape Optimization for a Low-Boom Demonstrator Concept", 33rd AIAA Applied Aerodynamics Conference, AIAA AVIATION Forum, AIAA 2015-2260.
[8] Ordaz, I., Wintzer, M., and Rallabhandi, S. K., "Full-Carpet Design of a Low-Boom Demonstrator Concept", 33rd AIAA Applied Aerodynamics Conference, AIAA AVIATION Forum, AIAA 2015-2261.
[9] Park, M. A. and Nemec, M., “Nearfield Summary and Statistical Analysis of the Second AIAA Sonic Boom Prediction Workshop” 35th AIAA Applied Aerodynamics Conference, AIAA AVIATION Forum, AIAA 2017-3256.
[10] Rallabhandi, S. K. and Loubeau, A., "Propagation Summary of the Second AIAA Sonic Boom Prediction Workshop", 35th AIAA Applied Aerodynamics Conference, AIAA AVIATION Forum, AIAA 2017-3257.
[11] Third Sonic Boom Workshop, Available: https://lbpw-ftp.larc.nasa.gov/sbpw3 [Accessed March 2020].
[12] Frink, N. T., Pirzadeh, S. Z, Parikh, P. C., Pandya, M. J., and Bhat, M. K., “The NASA Tetrahedral Unstructured Software System”, The Aeronautical Journal, Vol. 104, No. 1040, October 2000, pp. 491-499.
[13] Pandya, M. J., Frink, N. T., Ding, E., and Parlette, E. B., “Toward Verification of USM3D Extensions for Mixed Element Grids,” AIAA Paper 2013-2541.
[14] Pandya, M. J., Diskin, B., Thomas, J. L., and Frink, N. T., “Improved Convergence and Robustness of USM3D Solutions on Mixed Element Grids,” AIAA Journal, Vol. 54, No. 9, 2016, pp 2589-2610.
[15] Pandya, M. J., Diskin, B., Thomas, J. L., and Frink, N. T., “Assessment of USM3D Hierarchical Adaptive Nonlinear Iteration Method Preconditioners for Three Dimensional Cases,” AIAA Journal, Vol. 55, No. 10, 2017, pp 3409-3424.
[16] Pandya, M. J., Jespersen, D. C., Diskin, B., Thomas, J. L., and Frink, N. T., “Accuracy, Scalability, and Efficiency of Mixed-Element USM3D for Benchmark Three Dimensional Flows,” AIAA Paper 2019-2333.
[17] Durston, D. A., Cliff, S. E., Denison, M. F., Smith, N., Heineck, J. T., Schairer, E. T., Kushner, L. K., Castner, R. S., Elmiligui, A. A., Carter, M. B., Winski, C. S., Shea, P. R, and Blumenthal, B. T., “Nozzle Plume/Shock Interaction Sonic Boom Test Results from the NASA Ames 9- by 7-Foot Supersonic Wind Tunnel.” AIAA 2017-0041, January 2017.
[18] Winski, C. S., Carter, M. B., Elmiligui, A. A., Pearl, J., Nayani, S., and Durston, D., “Computational and Experimental Study of Plume and Shock Interaction Effects on Sonic Boom in the NASA Ames 9x7 Supersonic Wind Tunnel.” 2018 AIAA Aerospace Sciences Meeting, AIAA 2018-0331.
[19] NASA Low-Boom Flight Demonstration. https://www.nasa.gov/X59.
[20] Harten, A., Lax, P. D., and van Leer, B., “On Upstream Differencing and Godunov-Type Scheme for Hyperbolic Conservation Laws,” SIAM Review, Vol. 25, No. 1, 1983, p. 35.
[21] Barth, T. J. and Jespersen, D. C., The design and application of upwind schemes on unstructured meshes, in: Proceedings of the 27th AIAA Aerospace Sciences Meeting, Reno, NV, Paper AIAA 89-0366, 1989.

[22] Venkatakrishnan, V., Convergence to Steady State Solutions of the Euler Equations on Unstructured Grids with Limiters. Journal of Computational Physics, vol. 118, no. 1, 1995, pp. 120–130.
[23] van Albada, G. D., van Leer, B., and Roberts, W. W., "A comparative study of computational methods in cosmic gas dynamics" Astronomy and Astrophysics, 108 (1982), pp. 76-84.
[24] Spalart, P. R. and Allmaras, S. R., "A One-Equation Turbulence Model for Aerodynamic Flows," Recherche Aerospatiale, No. 1, 1994, pp. 5–21.
[25] Allmaras, S. R., Johnson, F. T., and Spalart, P. R., "Modifications and Clarifications for the Implementation of the Spalart–Allmaras Turbulence Model," Seventh International Conference on Computational Fluid Dynamics, Paper ICCFD7-1902, Aug. 2012, http://www.iccfd.org/iccfd7/proceedings.html.
[26] Rallabhandi, S. K., "Advanced Sonic Boom Prediction Using the Augmented Burgers Equation", Journal of Aircraft, Vol. 48, No. 4 (2011), pp. 1245-1253.
[27] Stevens, S. S., "Perceived level of noise by Mark VII and decibels(E)," Journal of the acoustical society of America, Vol. 51, No. 2, 1972, pp. 575–601.
[28] Shepherd, K. P. and Sullivan, B. M., "A Loudness Calculation Procedure Applied to Shaped Sonic Booms," NASA Technical Paper 3134, 1991.
[29] Loubeau, A., Naka, Y., Cook, B. G., Sparrow, V. W., and Morgenstern, J. M., "A New Evaluation of Noise Metrics for Sonic Booms Using Existing Data," 2nd International Sonic Boom Forum, 20th International Symposium on Nonlinear Acoustics, July 2015.
[30] Carter, M. B. and Park, M. A., "Near Field Summary and Analysis of the Third AIAA Sonic Boom Prediction Workshop.
[31] Shock-Plume Interaction Case," to be presented at AIAA Scitech 2021.
[32] HeldenMesh v3.0: https://heldenaero.com/heldenmesh.
[33] Park, M. A. and Carter, M. B., "Nearfield Summary and Analysis of the Third AIAA Sonic Boom Prediction Workshop C608 Low Boom Demonstrator" to be presented at AIAA SciTech 2021.
[34] Park, M. A., Campbell, R. L., Elmiligui, A. A., Cliff, S. E., and Nayani, S., "Specialized CFD Grid Generation Methods for Near-Field Sonic Boom Prediction" http://dx.doi.org/10.2514/6.2014-0115.